Syntheses, structures and properties of a series of inorganic–organic hybrid copper–lanthanide heterometal comprising germanotungstates with mixed ligands

Longhui Sun[a], Yajie Liu[a], Xiuhua Wang[a], Hailou Li[a], Jie Luo[a], Lijuan Chen[a,**], Junwei Zhao[a,b,*]

[a] Henan Key Laboratory of Polyoxometalate Chemistry, Institute of Molecular and Crystal Engineering, College of Chemistry and Chemical Engineering, Henan University, Kaifeng, Henan 475004, PR China
[b] State Key Laboratory of Structural Chemistry, Fujian Institute of Research on the Structure of Matter, Chinese Academy of Sciences, Fuzhou, Fujian 350002, PR China

ABSTRACT

The hydrothermal reaction of $K_8Na_2[A-\alpha-GeW_9O_{34}]\cdot25H_2O$, $Cu(CH_3COO)_2\cdot H_2O$, $Ln(NO_3)\cdot6H_2O$ and ethylenediamine (en) has led to a series of inorganic–organic hybrid copper–lanthanide heterometal comprising germanotungstates (GTs) $[Cu(en)_2(H_2O)]_6[Ln(H_2O)(CH_3COO)(\alpha-GeW_{11}O_{39})]_2\cdot8H_2O$ [Ln = Nd^{3+} (**1**), Sm^{3+} (**2**), Eu^{3+} (**3**), Gd^{3+} (**4**), Dy^{3+} (**5**), Ho^{3+} (**6**)], which have been characterized by elemental analyses, IR spectra, thermogravimetric (TG) analyses and single-crystal X-ray diffraction. Their common feature of **1–6** is that they all comprise a CH_3COO-bridging mono-Ln substituted dimeric GT fragment $[Ln(H_2O)(CH_3COO)(\alpha-GeW_{11}O_{39})]_2^{12-}$ with six supporting $[Cu(en)_2(H_2O)]^{2+}$ complex cations. To the best of our knowledge, such monovacant Keggin-type GTs containing both Cu–Ln heterometal centers and mixed en and acetate ligands are very rare. The luminescence properties and the lifetime decay behavior of the solid sample of **3** have been intensively investigated at room temperature.

© 2016 Elsevier B.V. All rights reserved.

1. Introduction

Polyoxometalates (POMs) have been known for almost two centuries since Berzelius for the first time discovered $(NH_4)_3PMo_{12}O_{40}\cdot nH_2O$ by reaction of ammonium molybdate and phosphoric acid [1]. POMs, as an attractive and vast class of discrete anionic metal oxides, are usually established via the condensation of metal oxide polyhedra (MO_x, M = W^{VI}, Mo^{VI}, V^{V}, Nb^{V}, Ta^{V}, etc., $x = 4$–7) in the corner-, edge-, or face-sharing manners [2–8]. Due to their nucleophilic oxygen-enriched surfaces and high negative charges, lacunary POMs can be served as one type of excellent inorganic multidentate O-donor ligands for assembly of active transition–metal (TM) or lanthanide (Ln) centers into novel TM substituted POMs (TMSPs) or Ln substituted POMs (LSPs). Hitherto, a large number of TMSPs and LSPs with diverse metal nuclearties, beautiful structural topologies and an unmatched range of physical and chemical properties applicable to diverse areas of research such as electronics, optics, catalysis and magnetism have been reported [9–20]. In contrast, much less interest has been dedicated to POM-based TM–Ln heterometallic derivatives (PBTLHDs). In 2004, the first class of PBTLHDs $[Ln(H_2O)_5\{Ni(H_2O)\}_2As_4W_{40}O_{140}]^{21-}$ (Ln = Y^{3+}, Ce^{3+}, Pr^{3+}, Nd^{3+}, Sm^{3+}, Eu^{3+}, Gd^{3+}) were reported by Xu and co-workers [21]. From then on, exploring and discovering multifunctional PBTLHDs has gradually become an emerging research topic of POM chemistry owing to their potential applications in magnetism and catalysis as well as their intriguing architectures and topologies [22–25]. Apparently, it is comparatively difficult to explore appropriate synthetic conditions to prepare PBTLHDs because of two following major difficulties: (I) the disparate reaction activities of electrophilic Ln and TM cations with nucleophilic lacunary POM

---

precursors in a reaction system will create the unavoidable competition reaction environments, thus only one type of metal cations exist in the overcomes during the course of crystallization [26]; (II) Ln cations have high oxyphilic reactivity towards lacunary POM fragments and usually lead to the formation of amorphous precipitates, which makes the structural determination of overcomes become rather difficult [27,28]. To date, only a certain number of PBTLHDs have been obtained under the sustained endeavors of synthetic chemists [22–25,29–35]. Within this subfamily, relevant reports on TM–Ln heterometal comprising GTs (TLHCGTs) are very limited. For instance, in 2010 and 2011, Reinoso and coworkers respectively obtained two intriguing Weakley-type sandwich-type TLHCGTs [{Ce(H$_2$O)$_2$}$_2$Mn$_2$(B-α-GeW$_9$O$_{34}$)$_2$]$^{8-}$ with an unprecedented {Ce^{III}$_2$Mn^{III}$_2$O$_{20}$} rhomb-like core exhibiting dominant Ce^{III}–Mn^{III} ferromagnetic interactions [36] and [{Ce(OAc)}Cu$_3$(H$_2$O)(B-α-GeW$_9$O$_{34}$)$_2$]$^{11-}$ with an interesting {Ce^{IV}Cu^{II}$_3$O$_{18}$} rhomb-like core magnetically behaving as a triangular Cu$_3$ system with overall antiferromagnetic interactions [31] by reaction of Ce^{4+} ions and the preformed precursors [Mn$_4$(H$_2$O)$_2$ (B-β-GeW$_9$O$_{34}$)$_2$]$^{12-}$ or [Cu$_4$(H$_2$O)$_2$(B-α-GeW$_9$O$_{34}$)$_2$]$^{12-}$ at room temperature. At the same time, Reinoso et al. also discovered an unseen crown-shaped dodecameric aggregate comprising Ce^{3+} and Ni^{2+} cations [Ni (H$_2$O)$_6$]$_3$[K⊂K$_7$Ce$_{24}$Ge$_{12}$W$_{120}$O$_{456}$(OH)$_{12}$(H$_2$O)$_{64}$]$^{46-}$ from a one-pot reaction of Na$_2$WO$_4$·2H$_2$O, Ce(NO$_3$)$_3$·6H$_2$O, GeO$_2$ and NiCl$_2$·6H$_2$O in the CH$_3$COOH—CH$_3$CCONa buffer [37]. In 2012, our group reported a class of organic–inorganic hybrid magnetic {Cu$_3$LnO$_4$} cubane inserted GTs {[Cu$_3$Ln(en)$_3$(OH)$_3$(H$_2$O)$_2$] (α-GeW$_{11}$O$_{39}$)}$_2$$^{4-}$ (Ln = Eu^{3+}, Tb^{3+}, Dy^{3+}) constructed from two {Cu$_3$LnO$_4$} cubane anchored monovacant [α-GeW$_{11}$O$_{39}$]$^{8-}$ fragments via two W–O–Ln–O–W linkers [38]. In 2013, Yang et al. communicated a 3-D organic–inorganic hybrid TLHCGT [Ce$_2$(ox)$_3$(-H$_2$O)$_2$]$_2${[Mn(H$_2$O)$_3$]$_2$[Mn$_4$(GeW$_9$O$_{34}$)$_2$(H$_2$O)$_2$]}$^{8-}$ constituted by sandwich-type tetra-Mn- substituted GT units through mixed Mn^{2+} and Ce^{3+} linkers (ox = oxalate) [39]. In the same year, our lab reported two novel 1-D copper-bridging tetrahedral POM nanoclusters with tetrameric rare-earth cores and GT vertexes [Cu (en)$_2$]$_5$[Cu(en)$_2$(H$_2$O)]$_2$[RE$_4$Ge$_4$W$_{46}$O$_{164}$(H$_2$O)$_3$]$^{10-}$ (RE = Gd^{3+}, Y^{3+}) [39]. In 2014, our group separated a class of 1-D double chain TLHCGTs [Cu(dap)$_2$(H$_2$O)][Ln(H$_2$O)$_3$(α-GeW$_{11}$O$_{39}$)]$^{3-}$ (Ln = La^{3+}, Pr^{3+}, Nd^{3+}, Sm^{3+}, Eu^{3+}, Tb^{3+}, Er^{3+}) displaying apparent electro-catalytic activities for nitrite, bromate and hydrogen peroxide reduction [25]. However, to the best of our knowledge, relevant reports on the reactions of the [α-A-GeW$_9$O$_{34}$]$^{10-}$ precursor with TM and Ln cations in the presence of mixed ligands are underdeveloped, which not only offer us with an enormous challenge and a good opportunity, but also give us a great driving force to explore this domain. Under this background, as a part of our continuous exploitation on PBTLHDs [24,25,34,35,38], recently, we have initiated an investigation of Cu^{2+} and Ln^{3+} cations to react with the [α-A-GeW$_9$O$_{34}$]$^{10-}$ precursor in the simultaneous participation of acetate and en ligands under hydrothermal conditions. Great efforts have been made to attain this target, eventually, we obtained a class of inorganic–organic hybrid TLHCGTs [Cu(en)$_2$(H$_2$O)]$_6$[Ln(H$_2$O)(CH$_3$COO) (α-GeW$_{11}$O$_{39}$)]$_2$·8H$_2$O [Ln = Nd^{3+} (**1**), Sm^{3+} (**2**), Eu^{3+} (**3**), Gd^{3+} (**4**), Dy^{3+} (**5**), Ho^{3+} (**6**)], which were structurally characterized by elemental analyses, IR spectra, TG analyses and single-crystal X-ray diffraction. The striking structural characteristic is that **1**–**6** consist of an acetate-bridging mono-Ln substituted GT dimeric fragment [Ln(H$_2$O)(CH$_3$COO)(α-GeW$_{11}$O$_{39}$)]$_2$$^{12-}$ with six supporting [Cu (en)$_2$(H$_2$O)]$^{2+}$ complex cations. As far as we know, such TLHCGTs with mixed en and acetate ligands are very rare. Moreover, the photoluminescence properties and the lifetime decay behavior of the solid sample of **3** have been probed in detail at room temperature.

2. Experimental

2.1. Materials and physical measurements

All the chemical reagents were used as purchased without further purification and the trivacant precursor K$_8$Na$_2$[A-α-GeW$_9$O$_{34}$]·25H$_2$O was prepared as previously described and further identified by IR spectra [41,42]. Elemental analyses (C, H and N) were performed on a Perkin–Elmer 2400-II CHN S/O analyzer. Inductively coupled plasma atomic emission spectrometry (ICP-AES) was performed on a Perkin−Elmer Optima 2000 ICP-AES spectrometer. IR spectra were recorded from solid samples palletized with KBr on a Nicolet 170 SXFT-IR spectrometer in the range 4000–400 cm^{-1}. TG analyses were performed on a Mettler Toledo TGA/SDTA 851^e instrument with a heating rate of 10 °C min^{-1} from 25 to 700 °C under flowing N$_2$ atmosphere. Photoluminescence and lifetime spectra were recorded using a FLS 980 Edinburgh analytical instrument furnished by a 450 W xenon lamp and a μF900 high-energy microsecond flash lamp as the excitation sources.

2.2. Synthesis of [Cu(en)$_2$(H$_2$O)]$_6$[Nd(H$_2$O)(CH$_3$COO) (α-GeW$_{11}$O$_{39}$)]$_2$·8H$_2$O (**1**)

Cu(CH$_3$COO)$_2$·H$_2$O (0.053 g, 0.265 mmol) and succinic acid (0.125 g, 1.06 mmol) were dissolved in 2 mL water forming a solution A; A aqueous solution (1 mL) containing Nd(NO$_3$)$_3$·6H$_2$O (0.202 g, 0.461 mmol), en (0.05 mL, 0.748 mmol) and NaCl (1 mol L^{-1}, 1 mL) was named as a solution B. Then A and B were added to another solution of K$_8$Na$_2$[A-α-GeW$_9$O$_{34}$]·25H$_2$O (0.217 g, 0.080 mmol) in 5 mL water. After vigorous stirring for 30 min, the pH value of the system was adjusted to 5.0 with solid sodium acetate (0.525 g, 3.858 mmol) and sodium hydroxide solution (4 mol L^{-1}). After stirring for another one hour, the mixture was sealed in a 25 mL Teflon-lined stainless steel autoclave, kept at 80 °C for 5 days and then cooled to room temperature. Purple lamellar crystals were obtained by filtering, washed with water and dried in air at ambient temperature. Yield: ca. 31% based on K$_8$Na$_2$[A-α-GeW$_9$O$_{34}$]·25H$_2$O. Anal. calcd (%) for C$_{28}$H$_{134}$Cu$_6$Ge$_2$N$_{24}$Nd$_2$O$_{98}$W$_{22}$: H, 1.87; C, 4.65; N, 4.65; Cu, 5.27; Ge, 2.01; Nd, 3.99; W, 55.90; Found: H, 1.98; C, 4.55; N, 4.48; Cu, 5.11; Ge, 2.20; Nd, 4.15; W, 55.77. IR (KBr pellets, cm^{-1}): 3436 (vs), 3318 (vs), 3270 (vs), 3150 (w), 2950 (w), 2891 (w), 1648 (m), 1591 (s), 1538 (m), 1428 (w), 1278(w), 1175 (w), 1096 (w), 1042 (s), 941 (vs), 874 (vs), 811 (vs), 689 (vs), 519 (s), 466 (s).

2.3. Synthesis of [Cu(en)$_2$(H$_2$O)]$_6$[Sm(H$_2$O)(CH$_3$COO) (α-GeW$_{11}$O$_{39}$)]$_2$·8H$_2$O (**2**)

2 was obtained using the similar procedure to **1**, except that Nd (NO$_3$)$_3$·6H$_2$O was replaced by Sm(NO$_3$)$_3$·6H$_2$O (0.200 g, 0.450 mmol). Yield ca. 32% based on K$_8$Na$_2$[A-α-GeW$_9$O$_{34}$]· 25H$_2$O. Anal. calcd (%) for C$_{28}$H$_{134}$Cu$_6$Ge$_2$N$_{24}$Sm$_2$O$_{98}$W$_{22}$: H, 1.86; C, 4.64; N, 4.64; Cu, 5.26; Ge, 2.00; Sm, 4.15; W, 55.81; Found: H, 1.95; C, 4.83; N, 4.50; Cu, 5.10; Ge, 2.14; Sm, 4.20; W, 55.64. IR (KBr pellets, cm^{-1}): 3435 (vs), 3318 (vs), 3265 (vs), 3150 (w), 2956(w), 2890 (w), 1641 (w), 1591 (s), 1537 (m), 1427 (w), 1278 (w), 1175 (w), 1097 (w), 1041 (s), 941 (vs), 872 (vs), 810 (vs), 687 (vs), 519 (s), 466 (s).

2.4. Synthesis of [Cu(en)$_2$(H$_2$O)]$_6$[Eu(H$_2$O)(CH$_3$COO) (α-GeW$_{11}$O$_{39}$)]$_2$·8H$_2$O (**3**)

The preparation of **3** is analogous to that of **1**, except that Nd (NO$_3$)$_3$·6H$_2$O was replaced by Eu(NO$_3$)$_3$·6H$_2$O (0.200 g, 0.448 mmol). Yield: ca. 38% based on K$_8$Na$_2$[A-α-GeW$_9$O$_{34}$]·

25H$_2$O. Yield ca. 32% based on K$_8$Na$_2$[A-α-GeW$_9$O$_{34}$]·25H$_2$O. Anal. calcd (%) for C$_{28}$H$_{134}$Cu$_6$Ge$_2$N$_{24}$Eu$_2$O$_{98}$W$_{22}$: H, 1.86; C, 4.64; N, 4.64; Cu, 5.26; Ge, 2.00; Eu, 4.19; W, 55.78; Found: H, 1.97; C, 4.67; N, 4.56; Cu, 5.17; Ge, 2.19; Eu, 4.09; W, 55.69. IR (KBr pellets, cm^{-1}): 3435 (vs), 3321 (vs), 3267 (vs), 3143 (w), 2956 (w), 2891(w), 1641 (w), 1590 (s), 1538 (m), 1425 (w), 1278 (w), 1175(w), 1097 (w), 1040 (s), 940 (vs), 873 (vs), 810 (vs), 687 (vs), 520 (s), 468 (s).

2.5. Synthesis of [Cu(en)$_2$(H$_2$O)]$_6$[Gd(H$_2$O)(CH$_3$COO)(α-GeW$_{11}$O$_{39}$)]$_2$·8H$_2$O (4)

The synthesis of **4** is similar to that of **1**, except that Nd(NO$_3$)$_3$·6H$_2$O was replaced by Gd(NO$_3$)$_3$·6H$_2$O (0.200 g, 0.443 mmol). Yield ca. 28% based on K$_8$Na$_2$[A-α-GeW$_9$O$_{34}$]·25H$_2$O. Anal. calcd (%) for C$_{28}$H$_{134}$Cu$_6$Ge$_2$N$_{24}$Gd$_2$O$_{98}$W$_{22}$: H, 1.86;

Table 1
Crystallographic data and structural refinements for **1–6**.

	1	2	3
Formula	C$_{28}$H$_{134}$Cu$_6$Ge$_2$N$_{24}$Nd$_2$O$_{98}$W$_{22}$	C$_{28}$H$_{134}$Cu$_6$Ge$_2$N$_{24}$Sm$_2$O$_{98}$W$_{22}$	C$_{28}$H$_{134}$Cu$_6$Eu$_2$Ge$_2$N$_{24}$O$_{98}$ W$_{22}$
Formula weight (g mol^{-1})	7235.19	7247.41	7250.63
T (K)	296	296	296
Crystal system	Monoclinic	Monoclinic	Monoclinic
Space group	$P2_1/c$	$P2_1/c$	$P2_1/c$
a (Å)	22.3378(12)	22.3272(19)	22.3188(12)
b (Å)	12.1901(6)	12.1695(10)	12.1725(6)
c (Å)	23.0594(12)	23.026(2)	23.0466(12)
α (°)	90	90	90
β (°)	95.7500(10)	95.896(2)	95.9190(10)
γ (°)	90	90	90
Unit cell volume (Å^3)	6247.5(6)	6223.3(9)	6227.8(6)
Z	2	2	2
D_c (g·cm^{-3})	3.846	3.868	3.867
Absorption coefficient (mm^{-1})	22.553	22.750	22.798
$F(000)$	6480	6488	6492
Crystal size (mm)	0.41 × 0.39 × 0.05	0.23 × 0.18 × 0.07	0.16 × 0.14 × 0.04
θ range for data collection (°)	1.78–25.00	1.78–25.00	1.78–25.00
Limiting indices	−26 ≤ h ≤ 25	−14 ≤ h ≤ 26	−25 ≤ h ≤ 26
	−14 ≤ k ≤ 13	−14 ≤ k ≤ 14	−14 ≤ k ≤ 14
	−25 ≤ l ≤ 27	−27 ≤ l ≤ 27	−24 ≤ l ≤ 27
Reflections collected	28448	31312	30662
Independent reflections	10769	10943	10753
R_{int}	0.0457	0.1102	0.0784
Max. and min. transmission	0.3985, 0.0390	0.2988, 0.0776	0.4624, 0.1214
Data/restraints/parameters	10,769/32/780	10,943/111/749	10,753/45/764
Goodness-of-fit on F^2	1.009	1.002	0.994
Final R ($I \geq 2\sigma(I)$)	$R_1 = 0.0560$	$R_1 = 0.0583$	$R_1 = 0.0449$
	$wR_2 = 0.1712$	$wR_2 = 0.1282$	$wR_2 = 0.0868$
Final R (all data)	$R_1 = 0.0661$	$R_1 = 0.1015$	$R_1 = 0.0730$
	$wR_2 = 0.1810$	$wR_2 = 0.1550$	$wR_2 = 0.0949$

	4	5	6
Formula	C$_{28}$H$_{134}$Cu$_6$Ge$_2$N$_{24}$Gd$_2$O$_{98}$W$_{22}$	C$_{28}$H$_{134}$Cu$_6$Ge$_2$N$_{24}$Dy$_2$O$_{98}$W$_{22}$	C$_{28}$H$_{134}$Cu$_6$Ho$_2$Ge$_2$N$_{24}$O$_{98}$ W$_{22}$
Formula weight (g mol^{-1})	7261.21	7271.71	7276.57
T (K)	296	296	296
Crystal system	Monoclinic	Monoclinic	Monoclinic
Space group	$P2_1/c$	$P2_1/c$	$P2_1/c$
a (Å)	22.3191(10)	22.3195(12)	22.3293(17)
b (Å)	12.1733(5)	12.1589(7)	12.1846(9)
c (Å)	23.0403(10)	23.0247(13)	23.0521(17)
α (°)	90	90	90
β (°)	95.9190(10)	96.1500(10)	95.910(2)
γ (°)	90	90	90
Unit cell volume (Å^3)	6226.5(5)	6212.5(6)	6238.5(8)
Z	2	2	2
D_c (g cm^{-3})	3.873	3.882	3.874
Absorption coefficient (mm^{-1})	22.860	22.912	23.021
$F(000)$	6496	6496	6508
Crystal size (mm)	0.25 × 0.15 × 0.07	0.50 × 0.10 × 0.05	0.15 × 0.12 × 0.07
θ range for data collection (°)	1.78–25.00	0.92–25.00	1.78–25.00
Limiting indices	−26 ≤ h ≤ 22	−24 ≤ h ≤ 26	−23 ≤ h ≤ 26
	−14 ≤ k ≤ 14	−14 ≤ k ≤ 14	−14 ≤ k ≤ 14
	−27 ≤ l ≤ 26	−27 ≤ l ≤ 23	−27 ≤ l ≤ 24
Reflections collected	30735	31107	31341
Independent reflections	10793	10930	10928
R_{int}	0.0597	0.0413	0.0804
Max. and min. transmission	0.2975, 0.0695	0.3937, 0.0308	0.2956, 0.1297
Data/restraints/parameters	10,793/40/754	10,930/16/749	10,928/65/765
Goodness-of-fit on F^2	1.028	1.036	1.008
Final R ($I \geq 2\sigma(I)$)	$R_1 = 0.0381$	$R_1 = 0.0349$	$R_1 = 0.0486$
	$wR_2 = 0.0757$	$wR_2 = 0.0821$	$wR_2 = 0.054$
Final R (all data)	$R_1 = 0.0567$	$R_1 = 0.0462$	$R_1 = 0.0851$
	$wR_2 = 0.0807$	$wR_2 = 0.0902$	$wR_2 = 0.0946$

C, 4.63; N, 4.63; Cu, 5.25; Ge, 2.00; Gd, 4.33; W, 55.70; Found: H, 1.96; C, 4.52; N, 4.54; Cu, 5.18; Ge, 2.11; Gd, 4.19; W, 55.58. IR (KBr pellets, cm^{-1}): 3435(vs), 3320 (vs), 3270 (vs), 3150 (w), 2950 (w), 2891 (w), 1641 (w), 1591 (s), 1538 (m), 1427 (w), 1278 (w), 1176 (w), 1095 (w), 1041 (s), 941 (vs), 874 (vs), 812 (vs), 688 (vs), 516 (s), 466 (s).

2.6. Synthesis of $[Cu(en)_2(H_2O)]_6[Dy(H_2O)(CH_3COO)(\alpha\text{-}GeW_{11}O_{39})]_2 \cdot 8H_2O$ (5)

The preparation of **5** is analogous to that of **1**, except that Nd(NO$_3$)$_3$·6H$_2$O was replaced by Dy(NO$_3$)$_3$·6H$_2$O (0.204 g, 0.447 mmol). Yield ca. 33% based on K$_8$Na$_2$[A-α-GeW$_9$O$_{34}$]·25H$_2$O. Anal. calcd (%) for C$_{28}$H$_{134}$Cu$_6$Ge$_2$N$_{24}$Dy$_2$O$_{98}$W$_{22}$: H, 1.86; C, 4.62; N, 4.62; Cu, 5.24; Ge, 2.00; Dy, 4.47; W, 55.62; Found: H, 1.90; C, 4.67; N, 4.56; Cu, 5.08; Ge, 2.13; Dy, 4.22; W, 55.73. IR (KBr pellets, cm^{-1}): 3437 (vs), 3322 (vs), 3270 (vs), 3142 (w), 2957 (w), 2889 (w), 1639 (m), 1591 (s), 1539 (w), 1427 (w), 1280 (w), 1175 (w), 1097 (w), 1041 (s), 942 (vs), 874 (vs), 813 (vs), 689 (vs), 519 (s), 468 (s).

2.7. Synthesis of $[Cu(en)_2(H_2O)]_6[Ho(H_2O)(CH_3COO)(\alpha\text{-}GeW_{11}O_{39})]_2 \cdot 8H_2O$ (6)

6 was produced in a similar procedure to **1**, except that Nd(NO$_3$)$_3$·6H$_2$O was replaced by Ho(NO$_3$)$_3$·6H$_2$O (0.208 g, 0.0453 mmol). Yield: ca. 26% based on K$_8$Na$_2$[A-α-GeW$_9$O$_{34}$]·25H$_2$O. Anal. calcd (%) for C$_{28}$H$_{134}$Cu$_6$Ge$_2$N$_{24}$Ho$_2$O$_{98}$W$_{22}$: H, 1.85; C, 4.62; N, 4.62; Cu, 5.24; Ge, 2.00; Ho, 4.53; W, 55.58; Found: H, 1.77; C, 4.76; N, 4.50; Cu, 5.09; Ge, 1.89; Ho, 4.34; W, 55.49. IR (KBr pellets, cm^{-1}): 3436 (vs), 3319 (vs), 3369 (vs), 3144 (w), 2950 (w), 2891 (w), 1641 (m), 1591 (s), 1538 (m), 1429 (w), 1278 (m), 1181 (w), 1097 (w), 1041 (s), 940 (vs), 874 (vs), 810 (vs), 688 (vs), 518 (s), 466 (s).

2.8. X-ray crystallography

A suitable single crystal of **1–6** was chosen and glued to a thin glass fiber with epoxy resin under an optical microscope carefully to ensure that the single crystal sample erects on the glass fiber. Single crystal data for X-ray structural analysis were performed on a Bruker CCD Apex–II diffractometer with Mo Kα radiation (λ = 0.71073 Å) at 296 K. The direct methods and full–matrix least–squares refinements on F^2 were used to solve their structures using the SHELXL–97 program package [43]. Besides the absorption correction using the SADABS program [44], routine Lorentz polarization and empirical absorption corrections were also applied. No H atoms on water molecules were located from the difference Fourier map. The positions of H atoms attached to the C and N atoms were geometrically placed. All H atoms were refined isotropically as a riding mode using the default SHELXTL parameters. All non-H atoms were refined anisotropically except for some O, C, N atoms and water molecules. Crystallographical data and structural refinements of **1–6** are summarized in Table 1.

3. Results and discussion

3.1. Structure descriptions of 1–6

1–6 were made by the reaction of K$_8$Na$_2$[A-α-GeW$_9$O$_{34}$]·25H$_2$O, Cu(CH$_3$COO)$_2$·H$_2$O, Ln(NO$_3$)·6H$_2$O and en in the presence of succinic acid under 80 °C hydrothermal conditions. Subsequently, the reactions with the removal of succinic acid were explored under similar conditions, **1–6** were not obtained, which reveal the synergistic effect of succinic acid with other components in the formation of **1–6**. Similar phenomena have been previously encountered [45–47]. The effects of pH value on the formation of **1–6** have been carried out. Experimental results show that the pH values ranging from 4.7 to 5.5 are suitable to the formation of the products and pH = 5.0 is the most appropriate pH value to
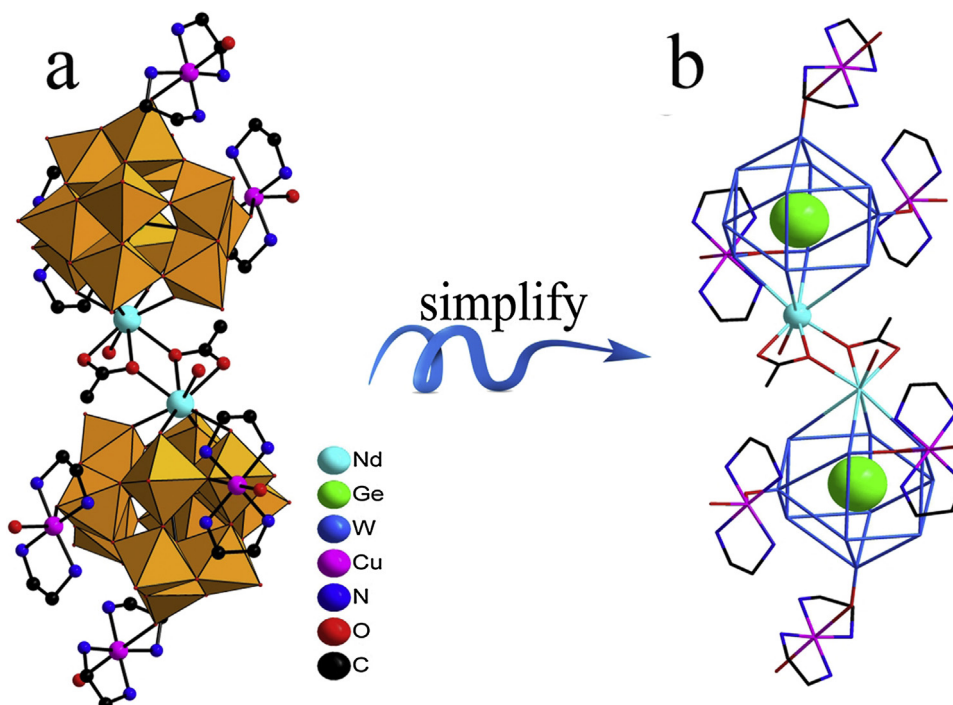
Fig. 1. (a) Combined ball-and-stick/polyhedral representation of the molecular structure of **1**. (b) The simplified view of the molecular structure of **1**.

acquire excellent crystals and good yields of **1–6**. In addition, the structures of **1–6** contain the monovacant Keggin $[\alpha\text{-GeW}_{11}O_{39}]^{8-}$ fragments although we used the trivacant Keggin $[\alpha\text{-GeW}_9O_{34}]^{10-}$ precursor as a starting material, indicating the conversion from $[\alpha\text{-GeW}_9O_{34}]^{10-}$ to $[\alpha\text{-GeW}_{11}O_{39}]^{8-}$ must have happened during the course of the formation of **1–6**.

Single-crystal X-ray diffraction indicates that organic–inorganic hybrids **1–6** are isomorphic and crystallize in the monoclinic $P2_1/c$ space group. Thus only the structure of **1** is described as an example. **1** consists of a dumbbell-shaped $[Nd(H_2O)(CH_3COO) (\alpha\text{-GeW}_{11}O_{39})]_2^{12-}$ dimeric unit, six butterfly-shaped $[Cu (en)_2(H_2O)]^{2+}$ coordination ions and eight water molecules of crystallization (Fig. 1a). Interestingly, the centrosymmetrical $[Nd (H_2O)(CH_3COO)(\alpha\text{-GeW}_{11}O_{39})]_2^{12-}$ dimeric unit can be deemed as a fusion of two equivalent $[Nd(H_2O)(CH_3COO)(\alpha\text{-GeW}_{11}O_{39})]^{6-}$ subunits through the bridging role of two $(\eta^2,\mu\text{-}1,1)$-acetate linkers (Fig. 1a,1b). This structural type of $[\{(\alpha\text{-SiW}_{11}O_{39}) Ln (COOCH_3)(H_2O)\}_2]^{12-}$ (Ln = Gd^{3+}, Yb^{3+}) was firstly found by Mialane and coworkers in 2004 during the course of exploring the reaction of monovacant Keggin silicotungstate with Ln cations in the CH_3COOH—CH_3COONa buffer solution [26]. Actually, this type of phosphotungstates $[\{(\alpha\text{-PW}_{11}O_{39})Ln(H_2O)(\eta^2,\mu\text{-}1,1)\text{-}CH_3COO\}_2]^{10-}$ (Ln = Sm^{3+}, Eu^{3+}, Gd^{3+}, Tb^{3+}, Ho^{3+}, Er^{3+}) was also prepared by Niu et al. in 2009 by reaction of the trivacant $[\alpha\text{-PW}_9O_{34}]^{9-}$ precursors with Ln cations in the participation of tetramethylammonium bromide in the CH_3COOH—CH_3COONa buffer solution [48]. It should be pointed out that their synthetic approaches are completely distinct although their types are almost the same. Specifically speaking, both $[\{(\alpha\text{-SiW}_{11}O_{39})Ln(COOCH_3)(H_2O)\}_2]^{12-}$ and $[\{(\alpha\text{-PW}_{11}O_{39})Ln(H_2O)(\eta^2,\mu\text{-}1,1)\text{-}CH_3COO\}_2]^{10-}$ were made in the CH_3COOH—CH_3COONa buffer solution by the conventional aqueous solution method [26,48] whereas $[Ln(H_2O)(CH_3COO)(\alpha\text{-GeW}_{11}O_{39})]^{6-}$ was synthesized by the one-pot hydrothermal reaction.

In the $[Nd(H_2O)(CH_3COO)(\alpha\text{-GeW}_{11}O_{39})]^{6-}$ subunit of **1**, the monovacant Keggin $[\alpha\text{-GeW}_{11}O_{39}]^{8-}$ fragment is constructed from a central tetrahedral $\{GeO_4\}$ group surrounded by three corner-shared $\{W_3O_{13}\}$ triads and an edge-shared $\{W_2O_{10}\}$ dimer. In each $\{W_3O_{13}\}$ triad, three $\{WO_6\}$ octahedra are fused together in the edge-shared mode. In the process of reaction, the conversion from the trivacant Keggin $[A\text{-}\alpha\text{-GeW}_9O_{34}]^{10-}$ to the monovacant $[\alpha\text{-GeW}_{11}O_{39}]^{8-}$ was observed, which can be regarded as that the trivacant Keggin precursor $[A\text{-}\alpha\text{-GeW}_9O_{34}]^{10-}$ incorporates two additional $\{WO_6\}$ octahedra into the defect sites (Fig. 2a) to form the monovacant $[\alpha\text{-GeW}_{11}O_{39}]^{8-}$ fragment. This transformation has been encountered during the course of our searching for PBTLHDs [25,38,40]. According to the previously reported results, some reaction rules can be deduced. When the trivacant Keggin $[A\text{-}\alpha\text{-GeW}_9O_{34}]^{10-}$ precursor is employed to make TLHCGTs under hydrothermal conditions, it tends to be transformed to the monovacant $[\alpha\text{-GeW}_{11}O_{39}]^{8-}$ fragment to incorporate a Ln^{3+} ion into the lacunary site [25,38,40] (Fig. 2b). On the contrary, in the conventional aqueous solution, the trivacant Keggin $[A\text{-}\alpha\text{-GeW}_9O_{34}]^{10-}$ precursor is easily isomerized to the $[B\text{-}\alpha\text{-GeW}_9O_{34}]^{10-}$ fragment to capture TM cations in the synthesis of TLHCGTs [31,36], because the $[A\text{-}\alpha\text{-GeW}_9O_{34}]^{10-}$ fragment possesses six exposed surface O atoms at each vacant site while the $[B\text{-}\alpha\text{-GeW}_9O_{34}]^{10-}$ fragment has seven exposed surface O atoms at each vacant site, thus the $[B\text{-}\alpha\text{-GeW}_9O_{34}]^{10-}$ fragment can function as a heptadentate ligand to bind TM cations and further enhance the stability of the resulting compounds [49]. In the $[Nd(H_2O)(CH_3COO)(\alpha\text{-GeW}_{11}O_{39})]^{6-}$ moiety, the Nd1^{3+} cation resides in an eight-coordinate square antiprism geometry and is combined with four lacunary O atoms from the $[\alpha\text{-GeW}_{11}O_{39}]^{8-}$ fragment [Nd–O: 2.365(11) −2.422(10) Å], three carboxylic O atoms from acetate groups [Nd–O: 2.510(11)–2.592(11) Å] and one coordinate water molecule [Nd–O: 2.536(14) Å] (Fig. 2c). These bond distances are in agreement with those observed in the known polyoxotungstates [50]. In the square antiprismatic geometry of the Nd1^{3+} cation, the
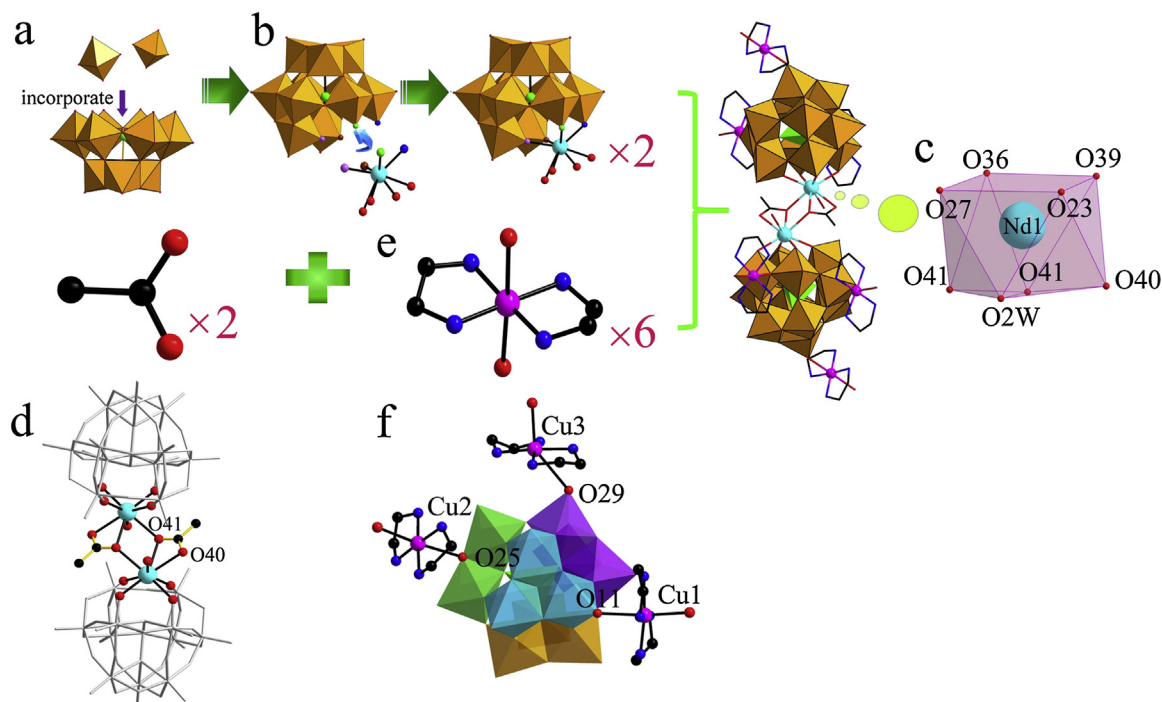
Fig. 2. (a) The trivacant Keggin precursor $[A\text{-}\alpha\text{-GeW}_9O_{34}]^{10-}$ and two additional $\{WO_6\}$ octahedral. (b) The schematic process of the monovacant $[\alpha\text{-GeW}_{11}O_{39}]^{8-}$ fragment encapsulating a Ln^{3+} ion into the lacunary site. (c) The square antiprismatic coordination environment of the Nd1^{3+} ion in **1**. (d) Combined ball-and-stick/wire view of the molecular structure of **1** with selected numbering scheme highlighting the connection between two Nd^{3+} ions by two acetate ligands. (e) The octahedral environments of the Cu1^{2+}, Cu2^{2+} and Cu3^{2+} ions in **1**. (e).

four unsaturated O atoms (O23, O27, O36, and O39) originating from the same $[\alpha\text{-GeW}_{11}\text{O}_{39}]^{8-}$ fragment constitute the upper plane while three carboxylic O atoms (O40, O41, O41A) and a water ligand (O2W) define the bottom plane. The average deviations of the upper plane and the bottom plane from their ideal planes are 0.0141 Å and 0.0765 Å, respectively. The distance between the Nd1^{3+} cation and the upper plane is 1.0316 Å whereas the distance between the Nd1^{3+} cation and the bottom plane is 1.6013 Å. The dihedral angle between the upper plane and the bottom plane is 4.9°. These structural data suggest that the square anti-prismatic geometry is highly distorted. It is worth noting that two Nd1^{3+} cations from adjacent two head-to-head [Nd(H$_2$O)(CH$_3$COO) (α-GeW$_{11}$O$_{39}$)]$^{6-}$ moieties are doubly bridged by two acetate ligands with the Nd···Nd distance of 4.223 Å. Apparently, albeit the two O atoms (O40 and O41) from the same one acetic ligand play a bridging role in the connection of two head-to-head [Nd(H$_2$O)(CH$_3$COO)(α-GeW$_{11}$O$_{39}$)]$^{6-}$ moieties, the coordination modes of the two O atoms of the acetate ligand are entirely different from each other: the O40 atom links to a carbon atom and a Nd^{3+} cation while the O41 atom is combined with two Nd^{3+} cations from two [Nd(H$_2$O)(CH$_3$COO)(α-GeW$_{11}$O$_{39}$)]$^{6-}$ moieties as well as a carbon atom (Fig. 2d). It can be explicitly seen that the distinction of the coordination mode of the two O atoms of the acetate ligand leads to the interesting (η^2,μ-1,1)-bridging mode of the acetate ligand.

As displayed in Fig. 1a, six butterfly-shaped [Cu(en)$_2$(H$_2$O)]$^{2+}$ supporting cations graft to the periphery of the dumbbell-shaped [Nd(H$_2$O)(CH$_3$COO)(α-GeW$_{11}$O$_{39}$)]$_2$$^{12-}$ dimeric unit by the terminal and bridging oxygen atoms on the $[\alpha\text{-GeW}_{11}\text{O}_{39}]^{8-}$ fragments. As a matter of fact, there are three crystallographically independent [Cu(en)$_2$(H$_2$O)]$^{2+}$ cations (namely, [Cu1(en)$_2$(H$_2$O)]$^{2+}$, [Cu2 (en)$_2$(H$_2$O)]$^{2+}$, [Cu3(en)$_2$(H$_2$O)]$^{2+}$) in the molecular unit. They all are embedded in the octahedral coordination geometry defined by four N atoms from two en ligands [Cu–N: 1.964(16)–2.048(19) Å] building the basal plane and a terminal or bridging O atom from the $[\alpha\text{-GeW}_{11}\text{O}_{39}]^{8-}$ fragment [Cu–O: 2.429(13)–3.287(11) Å] and a water ligand [Cu–O: 2.36(2)–2.493(21) Å] occupy two axial positions (Fig. 2e). Because of the existence of octahedral [Cu (en)$_2$(H$_2$O)]$^{2+}$ cations, the Cu–O elongated interactions derived from the evident Jahn-Teller distortion have been considered in the structural description [24,51], which can help to stabilize the structure [52]. In addition, a close inspection can be found that the coordination positions of three [Cu(en)$_2$(H$_2$O)]$^{2+}$ ions attaching to the $[\alpha\text{-GeW}_{11}\text{O}_{39}]^{8-}$ fragment are somewhat disparate: [Cu1 (en)$_2$(H$_2$O)]$^{2+}$ and [Cu3(en)$_2$(H$_2$O)]$^{2+}$ cations join to the $[\alpha\text{-GeW}_{11}\text{O}_{39}]^{8-}$ fragment via the terminal oxygen atoms, on the

contrast, the [Cu2(en)$_2$(H$_2$O)]$^{2+}$ cation grafts to the $[\alpha\text{-GeW}_{11}\text{O}_{39}]^{8-}$ fragment through a bridging oxygen atom (Fig. 2f).

It is noteworthy that the two $[\alpha\text{-GeW}_{11}\text{O}_{39}]^{8-}$ fragments in the [Nd(H$_2$O)(CH$_3$COO) (α-GeW$_{11}$O$_{39}$)]$_2$$^{12-}$ unit exhibit two types of spatial orientations (Fig. 3a). In order to highlight the spatial arrangement characteristic of 1, one spatial orientation is marked as A type and the other spatial orientation is denoted as B type, and then a simplified 2-D alignment with two kinds of spatial orientations is demonstrated in Fig. 3b. Viewed along the b axis, there also exist two kinds of spatial orientations for [Nd(H$_2$O)(CH$_3$COO)(α-GeW$_{11}$O$_{39}$)]$_2$$^{12-}$ units: one is toward the outside of plane (named as α), the other is toward the inside of plane (named as β). The arrangement modes of A and B units in α and β are seen in the highlighted rhombuses. Moreover, adjacent two spatial orientations for [Nd(H$_2$O)(CH$_3$COO)(α-GeW$_{11}$O$_{39}$)]$_2$$^{12-}$ units are staggered in the alternate fashion, which is contribute to reduce the steric hindrance as much as possible.

3.2. IR spectra of 1–6

IR spectra of 1–6 were recorded with a Nicolet 170 SXFT-IR spectrometer using KBr pellets in the range of 4000–400 cm^{-1} (Fig. S1). The characteristic vibration patterns resulting from Keggin-type GT framework mainly appear in the range of 1100–600 cm^{-1}. Four characteristic vibration bands attributable to ν(Ge–O$_a$), terminal ν(W–O$_t$), corner-sharing ν(W–O$_b$), and edge-sharing ν(W–O$_c$) asymmetric vibrations [25] appear at 874–872 cm^{-1} (874 cm^{-1} for 1, 872 cm^{-1} for 2, 873 cm^{-1} for 3, 874 cm^{-1} for 4, 874 cm^{-1} for 5, 874 cm^{-1} for 6), 942–940 cm^{-1} (941 cm^{-1} for 1, 941 cm^{-1} for 2, 940 cm^{-1} for 3, 941 cm^{-1} for 4, 942 cm^{-1} for 5, 940 cm^{-1} for 6), 813–810 cm^{-1} (811 cm^{-1} for 1, 810 cm^{-1} for 2, 810 cm^{-1} for 3, 812 cm^{-1} for 4, 813 cm^{-1} for 5, 810 cm^{-1} for 6), 689–687 cm^{-1} (689 cm^{-1} for 1, 687 cm^{-1} for 2, 687 cm^{-1} for 3, 688 cm^{-1} for 4, 689 cm^{-1} for 5, 688 cm^{-1} for 6), respectively. In comparison with the IR spectrum of the precursor K$_6$Na$_2$[(α-GeW$_{11}$O$_{39}$)]·13H$_2$O [41], the ν(W–O$_t$) vibration bands of 1–6 are almost not shifted, suggesting that [Cu(en)$_2$(H$_2$O)]$^{2+}$ cations have a weak effect on the terminal oxygen atoms of $[\alpha\text{-GeW}_{11}\text{O}_{39}]^{8-}$ fragments, which is in good consistence with the longer Cu–O distances [2.429(13)–3.287(11) Å] from the single-crystal X-ray diffraction analysis. The observation of the IR spectra of 1–6 obviously different from that of K$_8$Na$_2$[A-α-GeW$_9$O$_{34}$]·25H$_2$O [42] further consolidates the structural transformation from the [A-α-GeW$_9$O$_{34}$]$^{10-}$ precursor to the $[\alpha\text{-GeW}_{11}\text{O}_{39}]^{8-}$ fragment in the
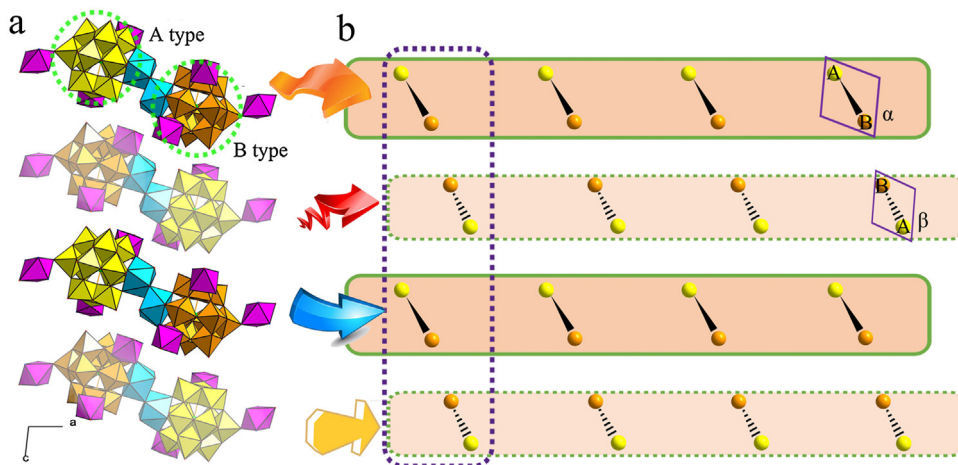
Fig. 3. Two types of spatial orientations of two $[\alpha\text{-GeW}_{11}\text{O}_{39}]^{8-}$ fragments in the [Nd(H$_2$O) (CH$_3$COO)(α-GeW$_{11}$O$_{39}$)]$_2$$^{12-}$ unit. (b) The simplified 2-D alignment with two kinds of spatial orientations.

formation of **1–6**. In the high wave-number region, the broad absorption band at 3436 cm^{-1} is attributed to the stretching vibrations of lattice and coordinated water molecules. Generally, the carboxylic group is anticipated to give very intense absorption bands from asymmetric vibration ($\nu_{asym}(CO_2^-)$, 1500–1630 cm^{-1}) and symmetric ($\nu_{sym}(CO_2^-)$, 1350–1460 cm^{-1}) stretching vibration [53,54]. In the IR spectra of **1–6**, the asymmetric $\nu_{asym}(CO_2^-)$ vibration and the symmetric $\nu_{sym}(CO_2^-)$ vibration derived from the acetate ligands are also seen at 1593–1589 cm^{-1} and 1463–1425 cm^{-1}, respectively. Moreover, the difference [$\Delta\nu = \nu_{asym}(CO_2^-) - \nu_{sym}(CO_2^-)$] between $\nu_{asym}(CO_2^-)$ and $\nu_{sym}(CO_2^-)$ in the IR spectrum has usually been used to judge the bonding modes of CO_2^- groups [55,56]. Generally speaking, when $\Delta\nu$ is greater than 200 cm^{-1}, CO_2^- groups utilize the monodentate fashion. In **1–6**, the values of $\Delta\nu$ (from 168 cm^{-1} to 126 cm^{-1}) indicate the chelating coordination modes of CO_2^- groups of acetate ligands. In addition, the resonances at 3322–3142 cm^{-1} and 2957–2950 cm^{-1} are assigned to the $\nu(NH_2)$ and $\nu(CH_2)$ stretching vibrations, and the signals at 1591–1590 cm^{-1} and 1429–1425 cm^{-1} correspond to the $\delta(NH_2)$ and $\delta(CH_2)$ bending vibrations, respectively. The occurrence of these resonance signals confirms the existence of en groups [38]. In short, the results of the IR spectra coincide with the single-crystal structural analyses.

3.3. Thermogravimetric properties of **1–6**

To examine the thermal stability of **1–6**, the TG analyses were performed under flowing dry nitrogen atmosphere with temperature ranging from 25 to 700 °C (Fig. 4). All the TG curves of **1–6** exhibit two weight loss steps. In the case of **1**, the first weight loss of 4.00% (calcd. 3.98%) between 25 and 147 °C, corresponds to the loss of eight crystal water molecules and eight coordinate water molecules. With further heating, the second step weight loss of 11.45% (calcd. 11.60%) from 147 to 700 °C involves the release of twelve en and two acetate ligands. For **2**, the first weight loss of 3.66% (calcd. 3.97%) from 25 to 132 °C assigned to the removal of eight crystal water molecules and eight coordinate water molecules. From 132 to 700 °C, the second step weight loss occurs (exp. 10.82%, calcd. 11.58%) and is attributable to the release of twelve en and two acetate ligands. With regard to **3**, one weight loss of 3.83% between 25 and 136 °C is assigned to the release of eight crystal water molecules and eight coordination water molecules (calcd. 3.97%). The other weight loss of 10.96% (calcd. 11.58%) from 136 to 700 °C corresponds to the removal of twelve en and two acetate ligands. As for **4**, the weight loss of 3.95% during the first step from 25 to 130 °C involves the liberation of eight crystal water molecules and eight coordination water molecules (calc. 3.97%). On further heating, the second weight loss is 11.02% between 130 and 700 °C, corresponding to the removal of twelve en and two acetate ligands (calc. 11.56%). With reference to **5**, the first step of weight loss of 3.54% happening between 25 and 124 °C results from the loss of crystal water molecules and eight coordination water molecules (calcd. 3.96%). Above 124 °C, the weight loss of 10.73% up to 700 °C is assigned to the removal of twelve en and two acetate ligands (calcd: 11.54%). In terms of **6**, the first-step weight loss of 3.18% occurring from 25 to 131 °C corresponds to the loss of eight crystal water molecules and eight coordination water molecules (calcd 3.96%) while the second-step weight loss of 11.64% occurring from 131 to 700 °C is attributable to the removal of twelve en and two acetate ligands (calcd 11.53%). Obviously, the observed experimental values are inosculated with the theoretical values.

3.4. Photoluminescence properties of **3**

Recently, Ln-based luminescent materials have been extensively investigated because of their extensive applications in the diverse fields such as lasers, plasma displays, biomedical, sensing areas, luminescence imaging, NIR-emitting materials and light emitting diodes coupled with their high color purity, the narrow emission lines and potentially high internal quantum efficiency [57,58], which may be mainly related to the special electronic properties of Ln ions, that is, the good shielding of the 4f electrons by the outer 5s and 5p electrons leads to well-defined absorption and emission bands and Ln cations still keep their atomic properties upon complex formation [59]. It should be noted that the photoexcitation of the O → M (M = Mo or W) transitions of POM units are able to give rise to intramolecular energy transfer from the O → M excited states to the excited energy levels of Ln ions, which then sensitizes the emission of the Ln cations [60]. Since the intramolecular energy transfer from POMs to Ln cations can occur by means of LMCT transitions, the luminescent properties of some POM-based Ln derivatives have been studied by Yamase and other research groups [34]. As a result, the photoluminescence properties and lifetime decay behavior of the solid sample of **3** have been studied at room temperature. When excited under an ultraviolet light of 394 nm, **3** displays the reddish orange emission and the photoluminescence emission spectrum reveals four characteristic emission bands at 595, 619, 654 and 699 nm (Fig. 5a), which are respectively assigned to the $^5D_0 \rightarrow {}^7F_1$, $^5D_0 \rightarrow {}^7F_2$, $^5D_0 \rightarrow {}^7F_3$ and $^5D_0 \rightarrow {}^7F_4$ transitions of the Eu^{3+} cation [61]. Generally speaking, the intensity of the magnetic dipole $^5D_0 \rightarrow {}^7F_1$ transition is almost unchanged with the crystal field strength acting on the Eu^{3+} cation whereas the electric dipole $^5D_0 \rightarrow {}^7F_2$ transition is hypersensitive to the chemical bonds in the vicinity of the Eu^{3+} cation [62]. As is known to all that the $^5D_0 \rightarrow {}^7F_1$ and $^5D_0 \rightarrow {}^7F_2$ transitions are attractive because both are sensitive to the symmetry of the ligand

Fig. 4. The TG curves of **1–6**.
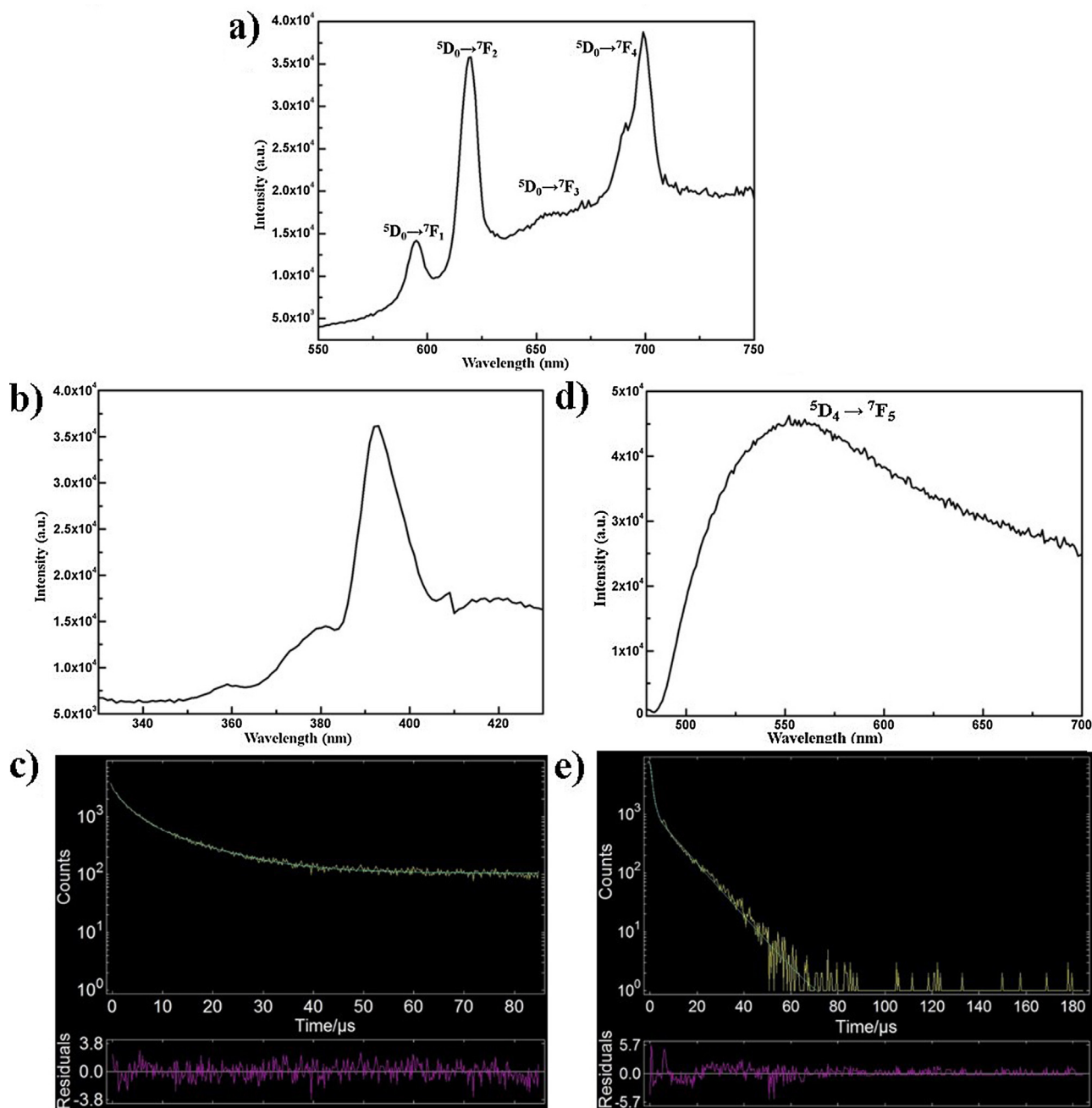
Fig. 5. (a) The emission spectrum of **3** under excitation at 394 nm at room temperature. (b) The excitation spectrum of **3** obtained by monitoring the emission at 619 nm. (c) The luminescence decay curve of **3**. (d) The luminescence decay curve of $K_6Na_2[(\alpha\text{-}GeW_{11}O_{39})]\cdot13H_2O$. (e) The emission spectrum of $K_8[\alpha\text{-}GeW_{11}O_{39}]\cdot nH_2O$ at room temperature.

field. The $^5D_0 \rightarrow {}^7F_1$ transition plays a predominant role in a centrosymmetric environment while the $^5D_0 \rightarrow {}^7F_2$ transition becomes the strongest in a noncentrosymmetric situation [63,64]. Furthermore, the intensity of the $^5D_0 \rightarrow {}^7F_2$ transition gradually increases as reducing the site symmetry of Eu^{3+} cation. As a consequence, the intensity ratio of $I(^5D_0 \rightarrow {}^7F_2)/I(^5D_0 \rightarrow {}^7F_1)$ is greatly sensitive to the local symmetry of the Eu^{3+} cation and is often utilized as a criterion of detecting the site symmetry of the Eu^{3+} cation [65]. In the emission spectrum of **3**, the intensity of the $^5D_0 \rightarrow {}^7F_2$ transition is much stronger than that of the $^5D_0 \rightarrow {}^7F_1$ transition with the intensity ratio of $I(^5D_0 \rightarrow {}^7F_2)/I(^5D_0 \rightarrow {}^7F_1)$ of ca. 4.5, indicating that the site symmetry of the Eu^{3+} cation in **3** is lower. In addition, the $^5D_0 \rightarrow {}^7F_4$ transition belongs to the

electric-dipolar transition and is also highly sensitive to the local microenvironments. In the case of **3**, the intensity of the $^5D_0 \rightarrow {}^7F_4$ transition also becomes stronger, which also further demonstrates that the Eu^{3+} cation is located at the low symmetry of the ligand field. The above observation is well coincident with the case that the Eu^{3+} cation inhabits in the highly distorted square antiprismatic geometry defined by four O atoms from a $[\alpha\text{-}GeW_{11}O_{39}]^{8-}$ subunits, three O atoms from two acetate ligands and a water ligand. Moreover, the dynamic coupling contribution can also help to the stronger intensity of $^5D_0 \rightarrow {}^7F_2$ and $^5D_0 \rightarrow {}^7F_4$ through the polarizability of the surrounding atoms [66,67]. In addition, by monitoring the $^5D_0 \rightarrow {}^7F_2$ emission at 619 nm, the excitation spectrum of **3** has been collected (Fig. 5b). The excitation spectrum

is dominated by a strong band at 392 nm, which is assigned to the $^7F_0 \rightarrow {}^5L_6$ transition. In the meantime, another three weak bands in the range of 340–420 nm are also seen in the excitation spectrum that involve in the intra-4f transitions from the $^7F_0$ ground state to higher energy levels of the Eu^{3+} cation, which are attributed to the $^7F_0 \rightarrow {}^5D_4$ (359 nm), $^7F_0 \rightarrow {}^5G_2$ (381 nm), $^7F_0 \rightarrow {}^5D_3$ (409 nm), respectively [68]. In order to determine the lifetime, the $^5D_0$ luminescence decay curve of the Eu^{3+} cation has been monitored under excitation at 394 nm and the most intense emission at 619 nm ($^5D_0 \rightarrow {}^7F_2$) (Fig. 5c). However, its decay curve can not be fitted to the single exponential function $I = A\exp(-t/\tau)$, but the double exponential function $I = A_1\exp(-t/\tau_1) + A_2\exp(-t/\tau_2)$ (where τ_1 and τ_2 are the fast and slow components of the lifetimes and A_1 and A_2 are the pre-exponential factors) affording the lifetimes τ_1 and τ_2 as 2.52 μs (28.78%) and 11.14 μs (71.22%), respectively. From the crystal structure of **3**, we can know that there is one crystallographically unique Eu^{3+} ion in **3**. Nevertheless, it is almost impossible that there are two different lifetimes for one crystallographically unique Eu^{3+} cation in **3**. To further investigate the origination of two different lifetimes, the luminescence decay curve of the monovacant Keggin GT $K_6Na_2[(\alpha\text{-}GeW_{11}O_{39})]\cdot 13H_2O$ has been also carried out (Fig. 5d) and can be fitted to a double exponential function with τ_1 and τ_2 of 0.99 μs (44.74%) and 9.62 μs (55.26%), respectively. This experimental result indicates that the lifetime of **3** indeed originates from the combined contributions of the Eu^{3+} ion and the $[\alpha\text{-}GeW_{11}O_{39}]^{8-}$ fragment. Moreover, the emission spectrum of the monovacant Keggin GT $K_6Na_2[(\alpha\text{-}GeW_{11}O_{39})]\cdot 13H_2O$ has been measured (Fig. 5e) and exhibits a broad emission band ranging from 480 nm to 700 nm that may derived from the $^3T_{1u} \rightarrow {}^1A_{1g}$ transitions from the O → W LMCT transitions. It can be clearly seen that the intensity of **3** is slightly weaker than that of $K_6Na_2[(\alpha\text{-}GeW_{11}O_{39})]\cdot 13H_2O$, which further suggests and supports that the intramolecular transfer of the O → W LMCT energy to the Eu^{3+} cation has indeed occurred during the course of the emission process of **3**, resulting in the appearance of two lifetimes of **3**. Therefore, the emission behavior of **3** mainly

stems from the common action of O → W LMCT transitions of GT fragments and the characteristic $^5D_0 \rightarrow {}^7F_J$ (J = 1–4) transitions of the Eu^{3+} cation. A good understanding of the true color is very important in the fields of lighting and display devices [69]. The CIE 1931 diagram is a widely used approach for probing all the possible colors by combining three primary colors, in which the chromaticity coordinates x and y are used to identify the precise emission colors of the as-synthesized materials. The CIE chromaticity coordinates for **3** and $K_6Na_2[(\alpha\text{-}GeW_{11}O_{39})]\cdot 13H_2O$ are determined based on their corresponding emission spectra and are indexed to (0.56018, 0.42549) and (0.43836, 0.53524), respectively (Fig. 6). It is clearly seen that **3** and $K_6Na_2[(\alpha\text{-}GeW_{11}O_{39})]\cdot 13H_2O$ exhibit the reddish orange and yellow-green emissions.

4. Conclusion

In summary, six inorganic–organic hybrid TLHCGTs $[Cu(en)_2(H_2O)]_6[Ln(H_2O)(CH_3COO)(\alpha\text{-}GeW_{11}O_{39})]_2\cdot 8H_2O$ $[Ln = Nd^{3+}$ (**1**), Sm^{3+} (**2**), Eu^{3+} (**3**), Gd^{3+} (**4**), Dy^{3+} (**5**), Ho^{3+} (**6**)] have been synthesized under 80 °C hydrothermal conditions, in which the interesting CH_3COO-bridging mono-Ln substituted dimeric GT fragment $[Ln(H_2O)(CH_3COO)(\alpha\text{-}GeW_{11}O_{39})]_2{}^{12-}$ is surrounded by six supporting $[Cu(en)_2(H_2O)]^{2+}$ complex cations. The thermal stability properties of **1–6** have been measured by TG analyses. Furthermore, the photoluminescence properties and the lifetime decay behavior of the solid sample of **3** have been discussed in detail. The photoluminescence emission behavior of **3** mainly stems from the combined contribution of the characteristic $^5D_0 \rightarrow {}^7F_J$ (J = 1–4) transitions of the Eu^{3+} cation and the O → W LMCT transitions of GT fragments. The luminescence decay curve of **3** can be well fitted to a double exponential function with τ_1 and τ_2 of 2.52 μs (28.78%) and 11.14 μs (71.22%), which is benefited from the synergistic action of the Eu^{3+} ions and the $[\alpha\text{-}GeW_{11}O_{39}]^{8-}$ fragments. By means of the CIE diagram, **3** and $K_6Na_2[(\alpha\text{-}GeW_{11}O_{39})]\cdot 13H_2O$ exhibit the reddish orange and yellow-green emissions. This research fruit not only enriches the structural diversity of PBTLHDs family, but also consolidates the one-pot hydrothermal reaction of lacunary POM precursors, Ln salts, TM salts and organic ligands is a robust strategy in synthesizing organic–organic hybrid PBTLHDs.

Appendix A. Supplementary data

Supplementary data associated with this article can be found, in the online version, at http://dx.doi.org/10.1016/j.synthmet.2016.04.008.

CCDC 1451594–1451599 contain the supplementary crystallographic data for this paper for six compounds. These data can be obtained free of charge from the Cambridge Crystallographic Data Centre via www.ccdc.cam.ac.uk/data_request/cif.
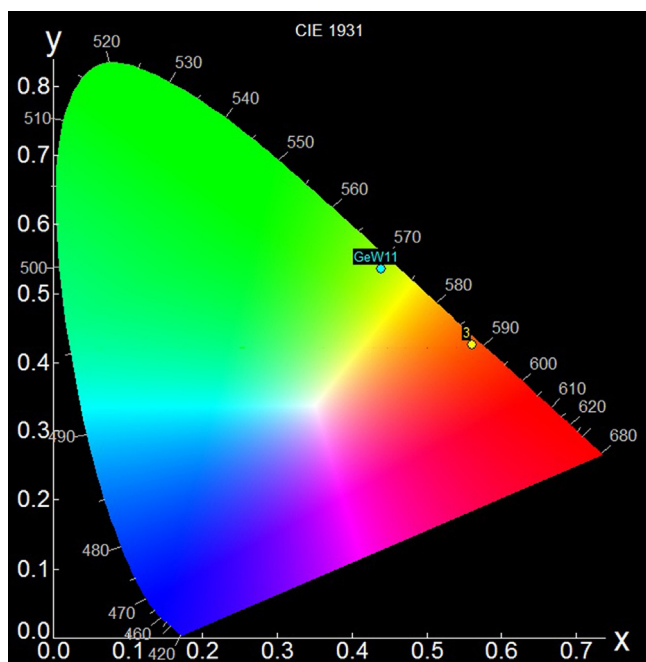
Fig. 6. The CIE chromaticity diagram of the emissions of **3** and $K_6Na_2[(\alpha\text{-}GeW_{11}O_{39})]\cdot 13H_2O$.

References

[1] J. Berzelius, Pogg. Ann. 6 (1826) 369.
[2] A. Proust, B. Matt, R. Villanneau, G. Guillemot, P. Gouzerh, G. Izzet, Chem. Soc. Rev. 41 (2012) 7605.
[3] D.L. Long, L. Cronin, Dalton Trans. 41 (2012) 9815.
[4] Y.F. Song, R. Tsunashima, Chem. Soc. Rev. 41 (2012) 7384.
[5] A. Udomvech, P. Kongrat, C. Pakawatchai, H. Phetmung, Inorg. Chem. Commun. 17 (2012) 132.
[6] P. Yin, G. Li, T. Liu, Chem. Soc. Rev. 41 (2012) 7368.
[7] L.C.W. Baker, D.C. Glick, Chem. Rev. 98 (1998) 3.
[8] A. Müller, F. Peters, M.T. Pope, D. Gatteschi, Chem. Rev. 98 (1998) 239.
[9] M. Du, C.-P. Li, M. Chen, Z.-W. Ge, X. Wang, L. Wang, C.-S. Liu, J. Am. Chem. Soc. 136 (2014) 10906.
[10] P. Mialane, A. Dolbecq, F. Sécheresse, Chem. Commun. 33 (2006) 3477.
[11] D.L. Long, R. Tsunashima, L. Cronin, Angew. Chem. Int. Ed. 49 (2010) 1736.
[12] J.M.C. Juan, E. Coronado, Coord. Chem. Rev. 193 (1999) 361.
[13] J.T. Rhule, C.L. Hill, D.A. Judd, R.F. Schinazi, Chem. Rev. 98 (1998) 327.
[14] A. Proust, R. Thouvenot, P. Gouzerhg, Chem. Commun. 16 (2008) 1837.
[15] C. Ritchie, A. Ferguson, H. Nojiri, H.N. Miras, Y.F. Song, D.L. Long, E. Burkholder, M. Murrie, P. Kögerler, E.K. Brechin, L. Cronin, Angew. Chem. Int. Ed. 47 (2008) 5609.
[16] A.E. Kuznetsov, Y.V. Geletii, C.L. Hill, K. Morokuma, D.G. Musaev, J. Am. Chem. Soc. 131 (2009) 6844.
[17] M.A. AlDamen, J.M. Clemente Juan, E. Coronado, C.M. Gastaldo, A.G. Ariño, J. Am. Chem. Soc. 130 (2008) 8874.
[18] J.D. Compain, P. Mialane, A. Dolbecq, I.M. Mbomekallé, J. Marrot, F. Sécheresse, E. Rivière, G. Rogez, W. Wernsdorfer, Angew. Chem. Int. Ed. 121 (2009) 3123.
[19] D. Barats, G. Leitus, R.P. Biro, L.J.W. Shimon, R. Neumann, Angew. Chem. Int. Ed. 47 (2008) 9908.
[20] L.J. Chen, D.Y. Shi, Y. Wang, H.L. Cheng, Z.D. Geng, J.W. Zhao, P.T. Ma, J.Y. Niu, J. Coord. Chem. 64 (2011) 400.
[21] H.Y. An, Y. Lan, Y.G. Li, E.B. Wang, N. Hao, D.R. Xiao, L.Y. Duan, L. Xu, Inorg. Chem. Commun. 7 (2004) 356.
[22] J.D. Compain, P. Mialane, A. Dolbecq, I.M. Mbomekallé, J. Marrot, F. Sécheresse, C. Duboc, E. Rivière, Inorg. Chem. 49 (2010) 2851.
[23] X.J. Feng, W.Z. Zhou, Y.G. Li, H.S. Ke, J.K. Tang, R. Clérac, Y.H. Wang, Z.M. Su, E.B. Wang, Inorg. Chem. 51 (2012) 2722.
[24] D.Y. Shi, J.W. Zhao, L.J. Chen, P.T. Ma, J.P. Wang, J.Y. Niu, CrystEngComm 14 (2012) 3108.
[25] J.W. Zhao, Y.Z. Li, F. Ji, J. Yuan, L.J. Chen, G.Y. Yang, Dalton Trans. 43 (2014) 5694.
[26] P. Mialane, A. Dolbecq, E. Riviére, J. Marrot, F. Sécheresse, Eur. J. Inorg. Chem. 2004 (2004) 33.
[27] C.D. Wu, C.Z. Lu, H.H. Zhuang, J.S. Huang, J. Am. Chem. Soc. 124 (2002) 3836.
[28] W.L. Chen, Y.G. Li, Y.H. Wang, E.B. Wang, Z.M. Zhang, Dalton Trans. 7 (2008) 865.
[29] D.Y. Shi, L.J. Chen, J.W. Zhao, Y. Wang, P.T. Ma, J.Y. Niu, Inorg. Chem. Commun. 14 (2011) 324.
[30] S. Reinoso, Dalton Trans. 40 (2011) 6610.
[31] S. Reinoso, J.R.G. Mascarós, L. Lezama, Inorg. Chem. 50 (2011) 9587.
[32] X.K. Fang, P. Kögerler, Chem. Commun. 29 (2008) 3396.
[33] B. Nohra, P. Mialane, A. Dolbecq, E. Rivière, J. Marrot, F. Sécheresse, Chem. Commun. 19 (2009) 2703.
[34] J.W. Zhao, J. Cao, Y.Z. Li, J. Zhang, L.J. Chen, Cryst. Growth Des. 14 (2014) 6217.
[35] L.J. Chen, F. Zhang, X. Ma, J. Luo, J.W. Zhao, Dalton Trans. 44 (2015) 12598.
[36] S. Reinoso, J.R. Galán-Mascarós, Inorg. Chem. 49 (2010) 377.
[37] S. Reinoso, M. Giménez-Marqués, J.R. Galán-Masarós, P. Vitoria, J.M. Gutiérrez-Zorrilla, Angew. Chem. Int. Ed. 49 (2010) 8384.
[38] J.W. Zhao, D.Y. Shi, L.J. Chen, Y.Z. Li, P.T. Ma, J.P. Wang, J.Y. Niu, Dalton Trans. 41 (2012) 10740.
[39] H.Y. Zhao, J.W. Zhao, B.F. Yang, H. He, G.Y. Yang, Cryst. Growth Des. 13 (2013) 5169.
[40] J.W. Zhao, D.Y. Shi, L.J. Chen, P.T. Ma, J.P. Wang, J. Zhang, J.Y. Niu, Cryst. Growth Des. 13 (2013) 4368.
[41] N. Haraguchi, Y. Okaue, T. Isobe, Y. Matsuda, Inorg. Chem. 33 (1994) 1015.
[42] L.H. Bi, U. Kortz, S. Nellutla, A.C. Stowe, Johan van Tol, N.S. Dalal, B. Keita, L. Nadjo, Inorg. Chem. 44 (2005) 896.
[43] G.M. Sheldrick, SHELXS-97, Program for Crystal Structure Solution, University of Göttingen, Germany, 1997.
[44] G.M. Sheldrick, SHELXL-97, Program for Crystal Structure Refinement, University of Göttingen, Germany, 1997.
[45] Z.M. Zhang, Y.G. Li, S. Yao, E.B. Wang, Y.H. Wang, R. Clérac, Angew. Chem. Int. Ed. 48 (2009) 1581.
[46] X.H. Wang, Q. Han, L.J. Chen, J.W. Zhao, Inorg. Chem. Commun. 63 (2016) 24.
[47] S.B. Tian, Y.Z. Li, J.W. Zhao, P.T. Ma, L.J. Chen, Inorg. Chem. Commun. 33 (2013) 99.
[48] J.Y. Niu, K.H. Wang, H.N. Chen, J.W. Zhao, P.T. Ma, J.P. Wang, M.X. Li, Y. Bai, Cryst. Growth Des. 9 (2009) 4362.
[49] J.-W. Zhao, H.-P. Jia, J. Zhang, S.-T. Zheng, G.-Y. Yang, Chem. Eur. J. 13 (2007) 10030.
[50] D.Y. Du, J.S. Qin, S.L. Li, Y.Q. Lan, X.L. Wang, Z.M. Su, Aust. J. Chem. 63 (2010) 1389.
[51] B.S. Bassil, S. Nellutla, U. Kortz, A.C. Stowe, J. van Tol, N.S. Dalal, B. Keita, L. Nadjo, Inorg. Chem. 44 (2005) 2659.
[52] B. Li, J.-W. Zhao, S.-T. Zheng, G.-Y. Yang, Inorg. Chem. 48 (2009) 8294.
[53] K.C. Szeto, K.P. Lillerud, M. Tilset, M. Bjørgen, C. Prestipino, A. Zecchina, C. amberti, S. Bordiga, J. Phys. Chem. B 110 (2006) 21509.
[54] S. Bordiga, C. Lamberti, G. Ricchiardi, L. Regli, F. Bonino, A. Damin, K.P. Lillerud, M. Bjorgen, A. Zecchina, Chem. Commun. 40 (2004) 2300.
[55] G.B. Deacon, R. Phillips, Coord. Chem. Rev. 33 (1980) 227.
[56] C.H. Li, K.L. Huang, Y.N. Chi, X. Liu, Z.G. Han, L. Shen, C.W. Hu, Inorg. Chem. 48 (2009) 2010.
[57] Y. Li, F.K. Zheng, X. Liu, W.Q. Zou, G.C. Gou, C.Z. Lu, J.S. Huang, Inorg. Chem. 45 (2006) 6308.
[58] J.C.G. Bünzli, C. Piguet, Chem. Soc. Rev. 34 (2005) 1048.
[59] G.J. Sopasis, M. Orfanoudaki, P. Zarmpas, A. Philippidis, M. Siczek, T. Lis, J.R. O'Brien, C.J. Milios, Inorg. Chem. 51 (2012) 1170.
[60] C. Ritchie, V. Baslon, E.G. Moore, C. Reber, C. Boskovic, Inorg. Chem. 51 (2012) 114.
[61] S.L. Cai, S.R. Zheng, Z.Z. Wen, J. Fan, W.G. Zhang, Cryst. Growth Des. 12 (2012) 5737.
[62] J.W. Zhao, H.L. Li, Y.Z. Li, C.Y. Li, Z.L. Wang, L.J. Chen, Cryst. Growth Des. 14 (2014) 5495.
[63] A.F. Kirby, F.S. Richardson, J. Phys. Chem. 87 (1983) 2544.
[64] J.W. Stouwdam, F.C.J.M. van Veggel, Nano Lett. 2 (2002) 733.
[65] T. Zhang, C. Spitz, M. Antonietti, C.F.J. Faul, Chem. Eur. J. 11 (2005) 1001.
[66] J. Rocha, L.D. Carlos, F.A.A. Paz, D. Ananias, Chem. Soc. Rev. 40 (2011) 926.
[67] O.L. Malta, L.D. Carlos, Quím Nova 26 (2003) 889.
[68] F.N. Shi, J. Meng, Y.F. Ren, Q. Su, J. Mater. Chem. 7 (1997) 773.
[69] Y. Zhang, W.T. Gong, J.J. Yu, H.C. Pang, Q. Song, G.L. Ning, RSC Adv. 5 (2015) 62527.